Combining active and passive seismic methods for the characterization of urban sites in Cairo, Egypt

Ashraf Adly,[1,2,3] Valerio Poggi,[3,4] Donat Fäh,[3] Awad Hassoup[1] and Awad Omran[2]

[1] *Seismology Department, National Research Institute of Astronomy and Geophysics, Egypt. E-mail: as_adly@yahoo.com*
[2] *Geology Department, Faculty of Science, Assiut University, Egypt*
[3] *Swiss Seismological Service, ETH Zurich, Switzerland*
[4] *Global Earthquake Model Foundation-GEM, Italy*

SUMMARY

The geology at Kottamiya, Rehab City and Zahraa–Madinat–Nasr to the East of Cairo (Egypt) is composed of low-velocity sediments on top of a rigid rock basement. Such sediments include the loose sands of the Gebel Ahmar formation, marl and shales of Maadi formation, in addition to sparse quaternary soil covers. Due to the contrast of the seismic impedance with the underlying bedrock, these soft sediments have the potential of considerably amplifying the ground motion during an earthquake. For the evaluation of site-specific seismic hazard, we computed the seismic site response in these areas by developing 1-D velocity models and derived average seismic velocities, including Vs_{30}. To do that, we applied different active and passive source techniques, including the horizontal to vertical Fourier spectral ratio of ambient vibration recordings and multichannel analysis of artificially generated surface waves. A set of models representing the velocity structure of the site is then obtained by combined inversion of Rayleigh wave dispersion curves and ellipticity functions. While dispersion curves are used to constrain the uppermost low-velocity part of the soil profile, ellipticity helps in resolving the structure at the depth of the sediment–bedrock interface. From the retrieved velocity models, numerical ground-motion amplification is finally derived using 1-D *SH*-wave transfer function. We account for uncertainty in amplification by using a statistical model that accounts for the misfit of all the inverted velocity profiles. The study reveals that the different sites experience an important frequency-dependent amplification, with largest amplification occurring at the resonance frequencies of the sites. Amplification up to a factor of 5 is found, with some variability depending on the soil type (Vs_{30} ranges between 340 and 415 m s^{-2}). Moreover, amplification is expected in the frequency range that is important for buildings (0.8–10 Hz), which is additional confirmation for the need of microzonation analysis of the area. The obtained results will be used for the development of a new seismic hazard model.

Key words: Joint inversion; Seismic noise; Site effects.

1 INTRODUCTION

The Cairo region (Egypt) has always been affected by moderate seismicity. Surprisingly, even rather small events have been capable to induce an unexpected level of destruction. This is the case for the 1992 Cairo swarm (with the largest event of moment magnitude M_w 5.9), causing at least 561 fatalities and injuring around 12 190 people (Abou Elenean *et al.* 2000). Such impact is due to the type and quality of local constructions, together with significant population density, but a non-negligible contribution is also likely coming from the presence of unfavourable local geological conditions, capable of inducing considerable amplification of the ground motion during an earthquake.

Evaluation of the local seismic response of this area is therefore key for earthquake risk mitigation and a proper resilience planning. Unfortunately, the amount of local information (geological and structural models) needed for the analysis is often financially unsustainable, due to elevated costs of invasive geological and geotechnical investigations (e.g. borehole drilling). Application of non-invasive geophysical techniques is a valid alternative for a reliable and cost-effective mapping of the subsoil properties over wide areas (e.g. Nakamura 1989; Bard 1998; Foti 2000; Bonnefoy-Claudet *et al.* 2009; Yoon 2011; Poggi *et al.* 2012). The

non-invasiveness of these methods is also desirable for densely populated areas. These advantages are particularly evident with geophysical techniques based on the analysis of ambient vibrations (also called passive methods, in contrast to standard active-source seismic techniques, Park *et al.* 1999; Dal Moro *et al.* 2003; Poggi *et al.* 2013), which became progressively more and more popular over the last two decades (Dravinski *et al.* 1996; Konno & Ohmachi 1998; Fäh *et al.* 2008; Endrun 2011).

In this study, we combine active and passive seismic methods to derive an estimate of the velocity structure at three selected locations within the Cairo urban area. We particularly focus on the topmost sedimentary cover and on the underlying bedrock interface. In particular, we make use of Rayleigh wave information (phase-velocity dispersion and ellipticity function) to constrain the velocity structure of the sites and resolve the location of the main seismic impedance contrast at depth. A two-step combined inversion approach is presented (e.g. Nagashima & Maeda 2005; Parolai *et al.* 2005; Picozzi *et al.* 2005), which directly descend from the technique proposed by Poggi *et al.* (2012) and extended herein to account for the uncertainty in the ellipticity function.

First, the velocity structure is resolved at a number of selected sites using surface wave dispersion from multichannel analysis of surface waves (MASW) analysis of active seismic recordings. Subsequently, the bedrock interface is mapped over the whole area by inverting Rayleigh ellipticity estimated from single-station measurements and assuming a homogenous velocity model. The 3-D model obtained in this way is finally the base for the calculation of numerical amplification using *SH*-wave transfer function formalism. Uncertainty in the ellipticity function is propagated through the inversion process using weighted misfit ranking of the velocity profiles and it is then used to produce an uncertainty model for the site amplification.

2 SOIL TYPES AND GEOLOGICAL SETTING

From the geological perspective, the sedimentary basin underlying eastern Cairo city consists of clastic loose deposits of Eocene to Quaternary age on top of a rigid limestone (Fig. 1). Those sediments comprise friable sands, shale, marl and some sparse basaltic patches.

Several formations are identified in the region, such as the Maadi, Gebel Ahmar and Hagul sediment units. The *Maadi formation* is composed of a succession of shale and marls accumulated during middle Eocene and outcropping at south Kottamiya. The Oligocenic *Gebel Ahmar formation* is mainly composed of loose sands and gravel, with occasional sparse patches of basaltic flows. These sediments are widely distributed in the Cairo-Suez District (the area from Cairo to the Gulf of Suez) and in the area at north Kottamiya (Stone park, Golf, west Golf and surrounding areas) and Zahraa. Sands are varicoloured, unstratified (usually loose or poorly cemented) and coarse grained. Colouration is due to uprising fluids carrying iron and manganese in the form of hot thermal springs through silicified tubes traversing the sand layer (Said 1992). *Hagul formation* was set down during the upper Miocene and represents the outcropping limestone sequence recognizable near the entrance of Wadi Hagul (at the north of the Gulf of Suez). This sedimentary sequence is widely distributed along the Cairo–Suez district and the western coast of the Gulf of Suez and is the main lithology under Rehab City. An additional layer of white to grey limestone is found close to this area, which seems to have been deposited in a so-called Heliopolis bay during Pliocene (Shukry & Ayouty 1956). *A Quaternary cover* of loose sands is sparsely distributed above the aforementioned formations.

3 FIELD ACQUISITION

3.1 Ambient vibration measurements

A total number of 117 single-station measurements were performed in the three areas at pre-defined locations (Fig. 2): 62 sites at Kottamiya, 21 sites at Zahraa and 34 sites at Rehab City. At each investigated point, ambient vibrations were recorded by using three-component seismological stations consisting of a 120 s sensor (Trillium compact) and a 24-bit high-resolution data logger (Taurus digital recorder). The use of long-period sensors was proven to be suboptimal in terms of acquisition efficiency. The long time needed
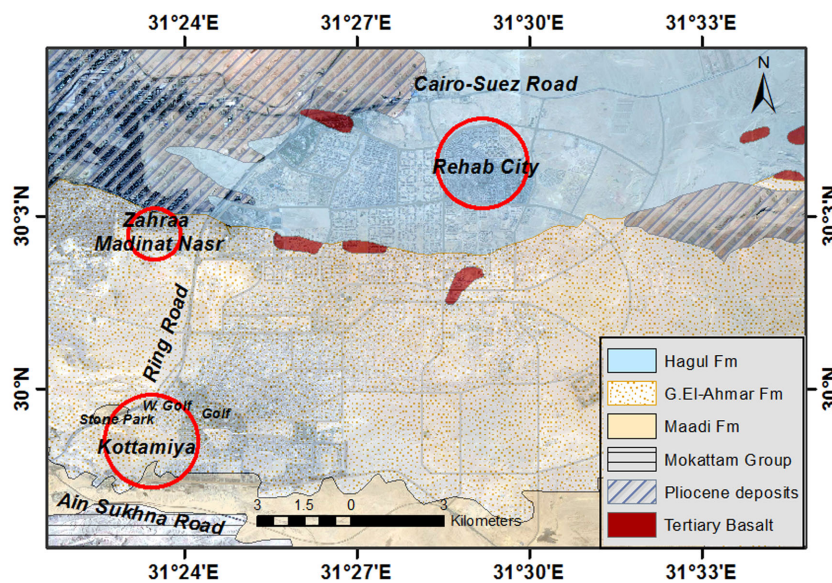
Figure 1. Map of surface geology showing the distribution of the lithological units over the study area; red circles mark the locations of the three investigated sites.
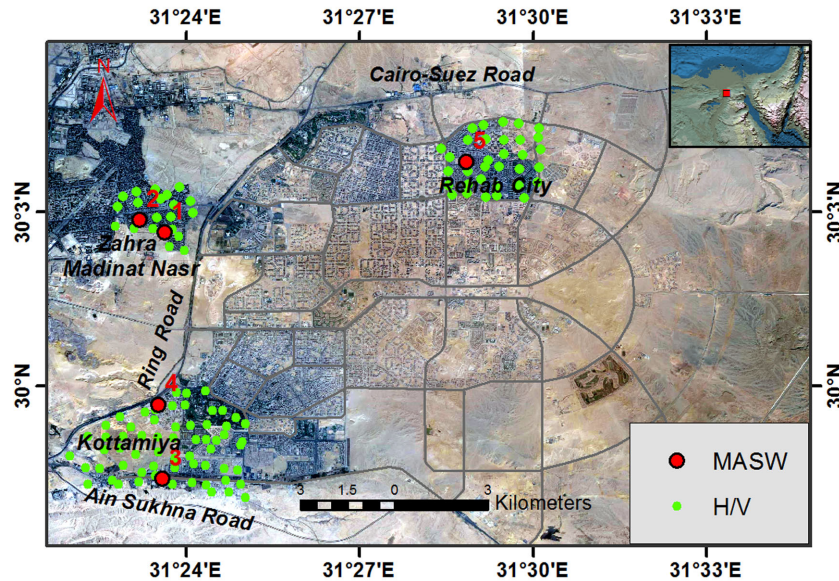
Figure 2. Location of H/V (in green) and MASW (in red) measurements at the three study areas. The red dot in the inset map refers to the relative location of study areas to neighbouring regions.

for the stabilization of the mass is practically not justified in the case of short-duration recordings (in this case less than one hour) and when only high frequency is the target (roughly > 0.2 Hz).

The distance between different measuring locations was set to be around 500 m, considered an optimal compromise between the need to cover such large areas and the available fieldwork time. In general, the weather conditions were favourable during most of the measurement time, with no rain and very few cases of strong wind, mostly during the acquisition in the Kottamiya region.

3.2 Active seismic experiments

Five active seismic experiments were performed in the region (Fig. 2). Two measurements were performed at Kottamiya on top of Maadi and Gebel Ahmar formations, two at Zahraa and the last one at Rehab City. The locations for the experiments were preventively chosen to highlight the possible variability of soil cover and outcropping bedrock. For the same reason, single-station ambient vibration recordings were distributed uniformly around the locations of the active seismic experiments, with the goal of subsequently performing joint analysis of active and passive data (surface wave dispersion and ellipticity curves, as it will be explained in the next sections).

Acquisition was carried out using digital multichannel seismograph (Nanometrix StrataView), with 24-bit analog-to-digital converter and dynamic range of 110 dB. The source equipment consisted of a 7 kg sledgehammer and a base metal plate to assure good coupling of the artificial source to the ground. A geophone string of 24 vertical elements with 4.5 Hz natural frequency was used to sample the wavefield at regular interval of 1 m (maximum spread length 23 m). The offset between the source and the array is 5 m. The recordings of five shots are stacked to increase the signal-to-noise ratio. The rather low natural frequency of the employed geophones is in general not necessary for most seismic applications (e.g. seismic refraction) where traveltimes are the target, but it is an essential requirement for the analysis of surface waves in frequency bands of engineering interest.

To account for the local potentially large variability of soil conditions in the near surface, the measurements were repeated 13 times
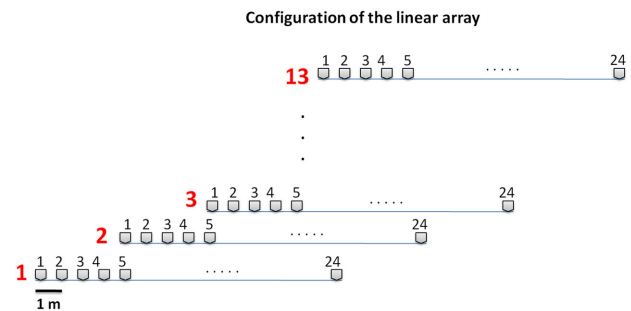
Figure 3. Schematic representation of array geometry used for the active seismic experiments; 24 geophones (4.5 Hz) are used with 1 m spacing. Several acquisitions are performed by progressively shifting the geophone string by 4 m.

by progressively shifting the whole array deployment of a 4 m interval. Therefore, the total length of the profile is 71 m (see Fig. 3 for an explicative sketch). This strategy allows estimating the average dispersion of surface waves over a wide area, therefore minimizing the chances of unfavourable measuring conditions.

4 AMBIENT VIBRATION ANALYSIS

4.1 H/V spectral ratios

The horizontal to vertical (H/V) Fourier spectral ratio is a seismic technique first introduced by Nogoshi & Igarashi (1971) and subsequently popularized by Nakamura (1989) that allows the empirical evaluation of fundamental period of resonance of a site. The method relies on polarization features of the seismic wavefield interacting with surface geology. It can be applied to either ambient vibrations (e.g. Konno & Ohmachi 1998; Bonnefoy-Claudet *et al.* 2009; Endrun 2011; Poggi *et al.* 2012) or actual earthquake recordings (Chavez-Garcia *et al.* 1996; Lachet *et al.* 1996), although its application to passive data became particularly widespread in the last decades. H/V technique is particularly suitable for rapid site characterization, as it requires a single three-component seismograph

and relatively short-duration recordings. In the case of ambient vibration, few tens of minutes are generally sufficient.

In case of structures with a large impedance contrast, the shape of H/V curves is largely controlled by the presence of surface waves in the wavefield (Lachet & Bard 1994; Fäh *et al.* 2001; Bonnefoy-Claudet *et al.* 2006; Haghshenas *et al.* 2008), with a minor contribution of body waves (e.g. Bonnefoy-Claudet *et al.* 2006) due to their rapid attenuation. Moreover, assuming similar contribution of body waves on the horizontal and vertical component of motions (true at least for limited frequency bands), their influence can be assumed negligible for practical purposes. Among surface waves, Rayleigh waves are supposedly mainly responsible for the development of maxima in the H/V spectra. These maxima are related to the polarized multimodal elliptical motion of Rayleigh waves in case of stratified media with significant velocity contrasts (e.g. Fäh *et al.* 2001, 2003; Malischewsky & Scherbaum 2004). The location of the first of these maxima has been demonstrated to be a good indicator (a proxy) for the site fundamental frequency (f_0). By removing the contribution of Love waves, H/V spectral ratio curves can closely approximate Rayleigh wave ellipticity function in specific frequency bands (Fäh *et al.* 2001). Based on array analysis, a number of studies (e.g. Tokeshi *et al.* 2000; Köhler *et al.* 2007; Endrun 2011; Poggi *et al.* 2012) have revealed a variability of Love-to-Rayleigh ratios at different sites. In some cases, Love waves can provide a significant contribution to the H/V peak amplitude, as the frequency of Love wave Airy phase can be comparable to the peak frequency of the fundamental-mode Rayleigh wave ellipticity function (Bonnefoy-Claudet *et al.* 2008). Recently, some trials were made to extract the Rayleigh wave's ellipticity function from the ambient vibration wave field using single stations (e.g. Hobiger *et al.* 2009, 2012, 2013; Poggi *et al.* 2012; Gouveia *et al.* 2016). However, we correct for the influence of Love waves through the assumption of equal energy partition between Love and Rayleigh waves in the horizontal plane. It has been demonstrated that such assumption works generally well in limited frequency bands (the so-called right flank, Fäh *et al.* 2001) and when the presence of other waves types, such as *SH* body waves, is small (Fäh *et al.* 2008). Though, this could result in an overestimation of Rayleigh waves in case of prevalence of Love waves and vice versa. We make use of this specific information to infer important information on soil structure, such as the location of bedrock interface, through a combined inversion strategy (Picozzi *et al.* 2005; Arai & Tokimatsu 2008; Ducellier *et al.* 2012; Poggi *et al.* 2012).

4.2 Processing parameters

In order to process H/V spectral ratios, the three component recordings of ambient vibration are preliminary processed by removing the long-period component of the wave field using a fifth-order causal high-pass Butterworth filter with corner at 0.2 Hz. The filtered recordings are subdivided in smaller time windows of 50 s and each window is then tapered using a cosine taper function in order to avoid development of spurious high-frequency artefacts in the results. H/V ratios are subsequently calculated for each window separately and the spectra smoothed using the Konno & Ohmachi (1998) algorithm with bandwidth coefficient of 40. The mean and standard deviation of H/V spectra are finally computed assuming lognormal statistics (e.g. Fig. 4).

It has to be mentioned that horizontal components are combined before computing spectral ratio using vector summation. After that, H/V spectra are scaled by a factor of square root of two, to tentatively
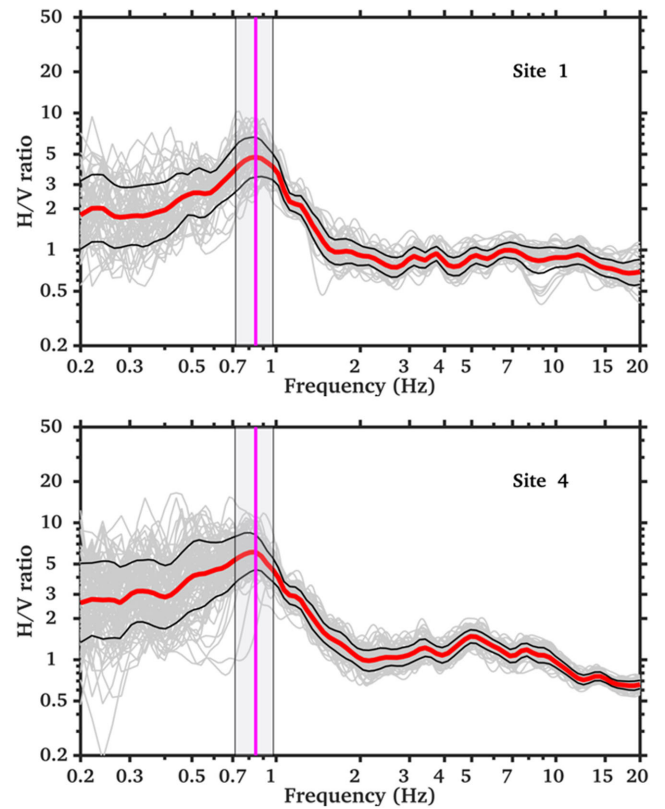

Figure 4. Mean H/V spectral ratio (in red) and the uncertainty of 1σ standard deviation (in black) at two sites. Purple lines denote f_0, and shaded light grey regions define its uncertainty.
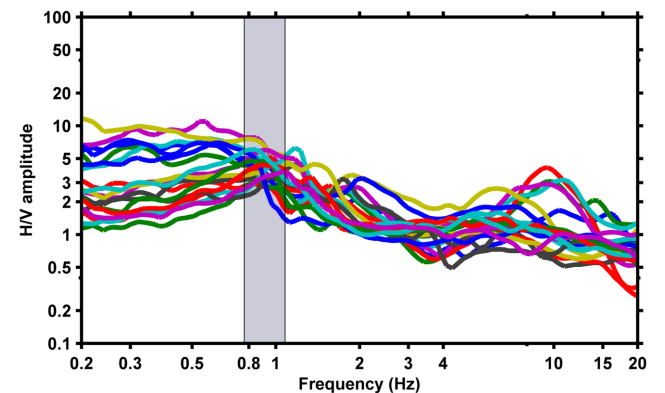

Figure 5. H/V curves measured at Kottamiya, high-frequency resonance peaks appear above 4 Hz at varying frequencies reflecting the variation in the depth of the shallow interface. Low-frequency peaks appear around 0.9 Hz. The grey region defines the fundamental frequency range.

correct for the Love waves contribution following the previous assumption of energy equally portioned between Love and Rayleigh waves (Fäh *et al.* 2001, 2003) at the right flank of the ellipticity first maximum.

4.3 Results

H/V spectral ratios were computed at the defined locations in the three study areas. From H/V spectra (Figs 5–7), site resonance frequencies have been identified by manually picking the largest maxima of the computed spectra.
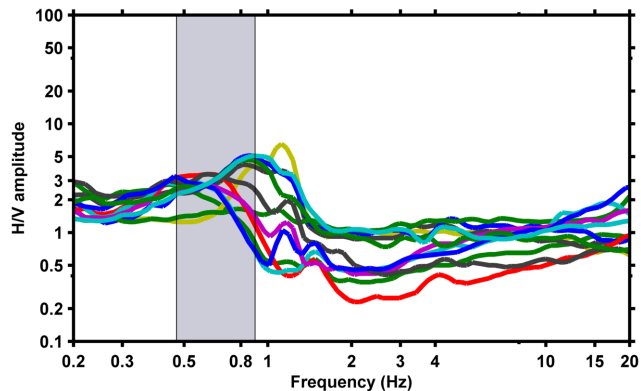
Figure 6. H/V Fourier spectral ratios for the ambient vibrations recorded at Zahraa exhibit peaks at the low-frequency; also, anthropogenic sharp peaks appear at around 1.1 Hz. The grey region defines the fundamental frequency range.

At Kottamiya site, H/V curves are characterized by the presence of two peaks: one at low frequency (around 0.8 Hz) and the other is at high—but less defined—frequency (Fig. 5).

However, some curves are characterized by flat (plateau-shaped) maxima at the low frequency, which may be induced by the windy conditions. Nonetheless, the plateau might also be interpreted by a mild influence of 2-D/3-D wave propagation phenomena (Uebayashi 2003; Bonnefoy-Claudet *et al.* 2009), an issue that is presently not fully solved and might require further investigations. The fundamental frequency of these curves is defined as the frequency at the right-hand side of the broad peak because this frequency coincides with the general resonance frequency of the area as indicated by curves with clear and sharp peaks. The low-frequency peaks are related to the impedance contrasts at the sediment–bedrock interface. On the other hand, the high-frequency peaks are consistently observed at the southern part of Kottamiya together with the low-frequency peaks. Therefore, these peaks are assumed to be related to a shallow interface with a sufficient impedance contrast and not induced by higher modes.

Relating these observations to the geology at Kottamiya, we can assume that the high-frequency peaks are related to the contact between Maadi formation and overlying sediments. These sediments may be related to the quaternary sediments or to Gebel Ahmar sands at some parts. The high-frequency peaks appear at varying frequencies between 4 and 20 Hz. The variability in the frequency of these peaks is an indication of spatial variation of the depth to the Maadi formation. On the other hand, the low-frequency peaks are related to the contact between the bedrock and the overlying Maadi formation at south Kottamiya. At north Kottamiya, the bedrock is overlain either just by Gabel Ahmar formation or by Maadi formation which is overlain by Gabel Ahmar formation.

At north Kottamiya (where the loose sands are outcropping), H/V curves are characterized the absence of high-frequency peaks. This is an evidence that the high-frequency peaks observed at south Kottamiya are related to the contact between Maadi formation and quaternary sediments. The low- and high-frequency peaks are manually picked and mapped (Fig. 8). Anthropogenic (industrial or unnatural) peaks show up at around 1.3 Hz, this is probably due to the machinery in the Kottamiya industrial zone and construction activities (e.g. concrete mixers and cement pump trucks) in the study areas. Such peaks can be easily identified on the spectrum, as their amplitude grows rapidly with decreasing level of smoothing, in addition to a typically small uncertainty.
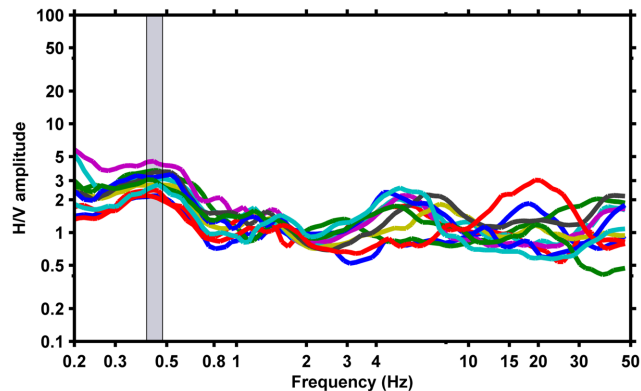
Figure 7. H/V spectral ratios at Rehab City, high-frequency peaks occur at varying frequencies, while the low-frequency peaks are at the same frequency reflecting a flat bedrock interface. The grey region defines the fundamental frequency range.

At Zahraa, H/V curves show only low-frequency peaks in the range 0.45–1 Hz (Fig. 6). The resonance frequency increases from north to south indicating a dipping bedrock interface where the depth of the sedimentary basin increases in the trend from south to north in a gradual fashion (Fig. 9). The general absence of high-frequency peaks is an indication of the homogeneity of sands (absence of sharp velocity contrasts). Similar to the case in Kottamiya, sharp artificial peaks are also identified at frequencies around 1.3 Hz. The gradual increase of the amplitude of these peaks can be used as an indicator to the direction of these sources but this is not an issue for this study.

The Rehab City is constructed on a thin layer of quaternary sediments overlying Hagul formation. Similar to the case in Kottamiya, the resonance peaks appear at high and low frequencies on H/V curves (Fig. 7): high-frequency peaks appear at variable frequencies (from 4 to more than 20 Hz) revealing the variability in the thickness of the shallow quaternary sediments. The highest frequency is observed at the eastern and central parts of Rehab City and decreases in other directions (Fig. 10). Frequencies of 20 Hz and higher (at shallow outcrops of Hagul formation) are represented by a fixed value of 20 Hz. On the other hand, the low-frequency peaks are stacked at almost the same frequency (Fig. 7) indicating a deep bedrock depth with small variation. The low-frequency peaks are mapped in Fig. 10.

5 ACTIVE SEISMIC EXPERIMENTS

5.1 Multichannel analysis of surface waves

Frequency wavenumber (*f-k*) analysis is a spectral technique based on multiple (array) recordings, which is widely used to decompose the seismic wave field into elementary wave contributions. The method is particularly suitable to extract phase-velocity dispersion information of the surface waves. Although initially thought for the analysis of earthquakes (e.g. Capon 1969), *f-k* methods have been subsequently extended to the analysis of wave fields from active experiments, for example, the MASW technique (e.g. Yilmaz 1987; Foti 2000; Kanli *et al.* 2006; Yoon 2011; Poggi *et al.* 2013), and later applied to passive recordings too (e.g. Roten & Fäh 2007; Arai & Tokimatsu 2008; Yoon 2011).

In our implementation, the frequency–velocity spectrum is obtained by applying beamforming algorithm as in Lacoss *et al.* (1969), which implies the calculation of the spectral
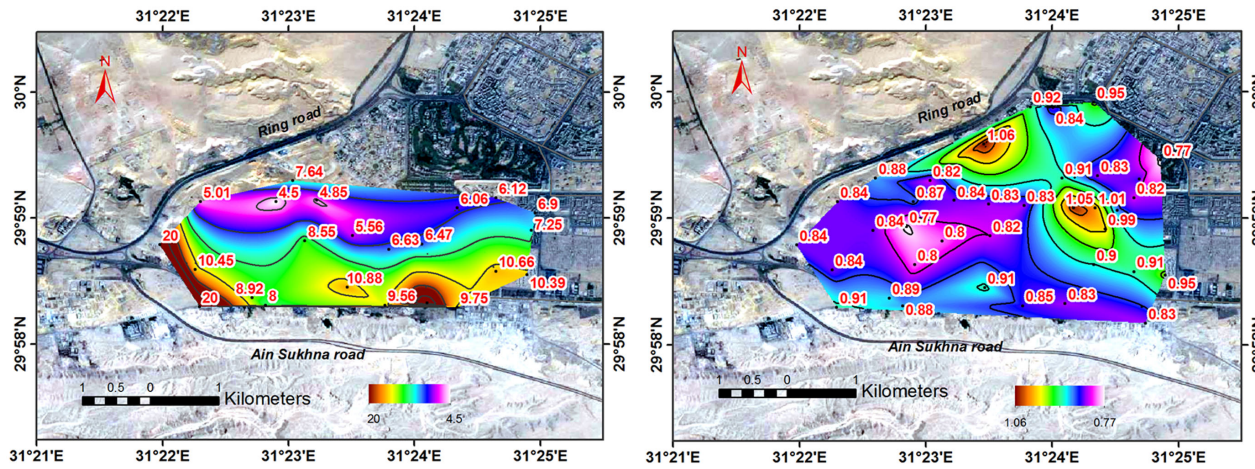
Figure 8. High- and low-frequency peaks at Kottamiya. The interpolation in some areas is tentative due the low density of measurement points.
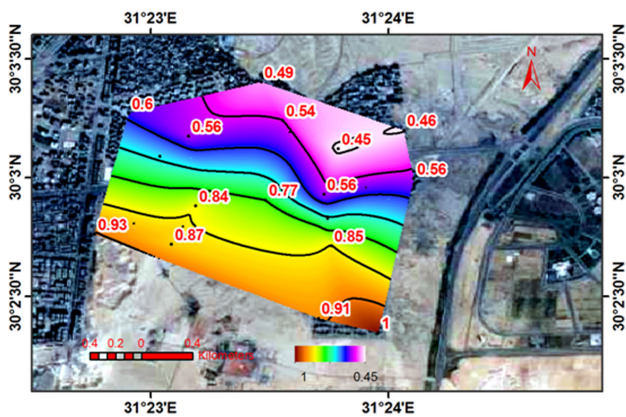

Figure 9. Low-frequency peaks at Zahraa, the fundamental frequency increases from north to south. The interpolation in some areas is tentative due the low density of measurement points.

cross-correlation matrix (CCM) to estimate signal's phase delay between receiver pairs. If compared to conventional *f-k* analysis (as a simple 2-D Fourier transform), the beamforming approach is advantageous as it allows the stack of the 13 CCM realizations from the successive shot gathers. This improves the quality of the phase velocity estimates by minimizing the effect of random uncorrelated noise (Poggi *et al.* 2012). Moreover, because the shots are taken in different nearby locations, the result can be considered representative of the average conditions across the area.

5.2 Results

Frequency–velocity power spectra have been computed in the frequency range between 5 and 100 Hz and for a velocity range between 100 and 1000 m s^{-1}. By visual inspection of the *v-f* spectra (Fig. 11), the Rayleigh wave phase velocity smoothly but constantly decreases toward high frequencies, which is a clear indication of homogeneity of the shallow sedimentary cover. This is generally the case in the investigated areas except at site 5, where there is a slightly more pronounced transition from low to high velocity.
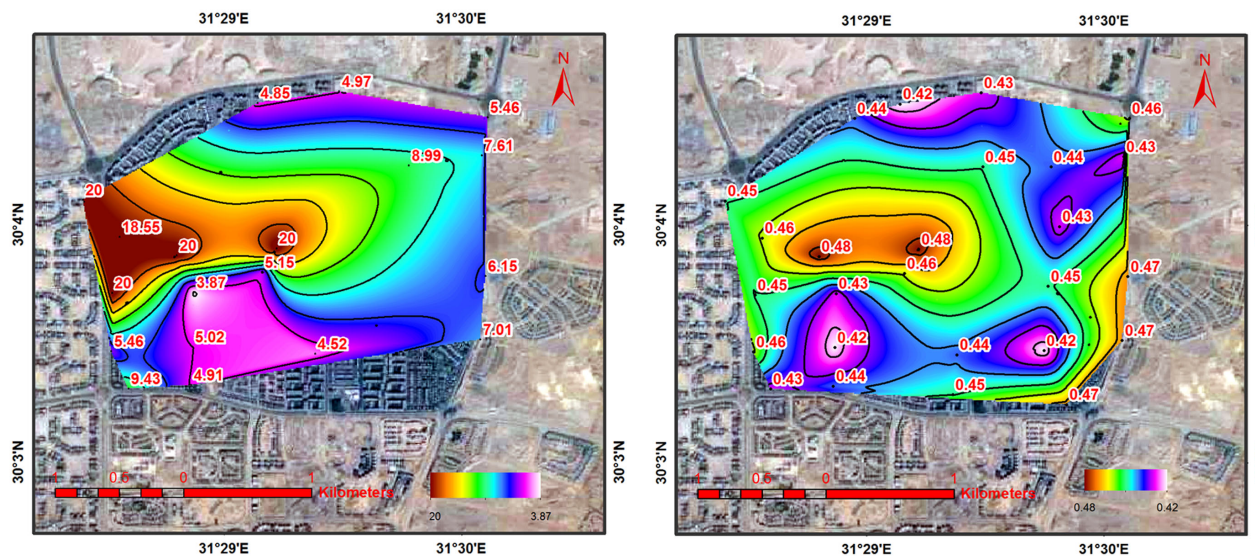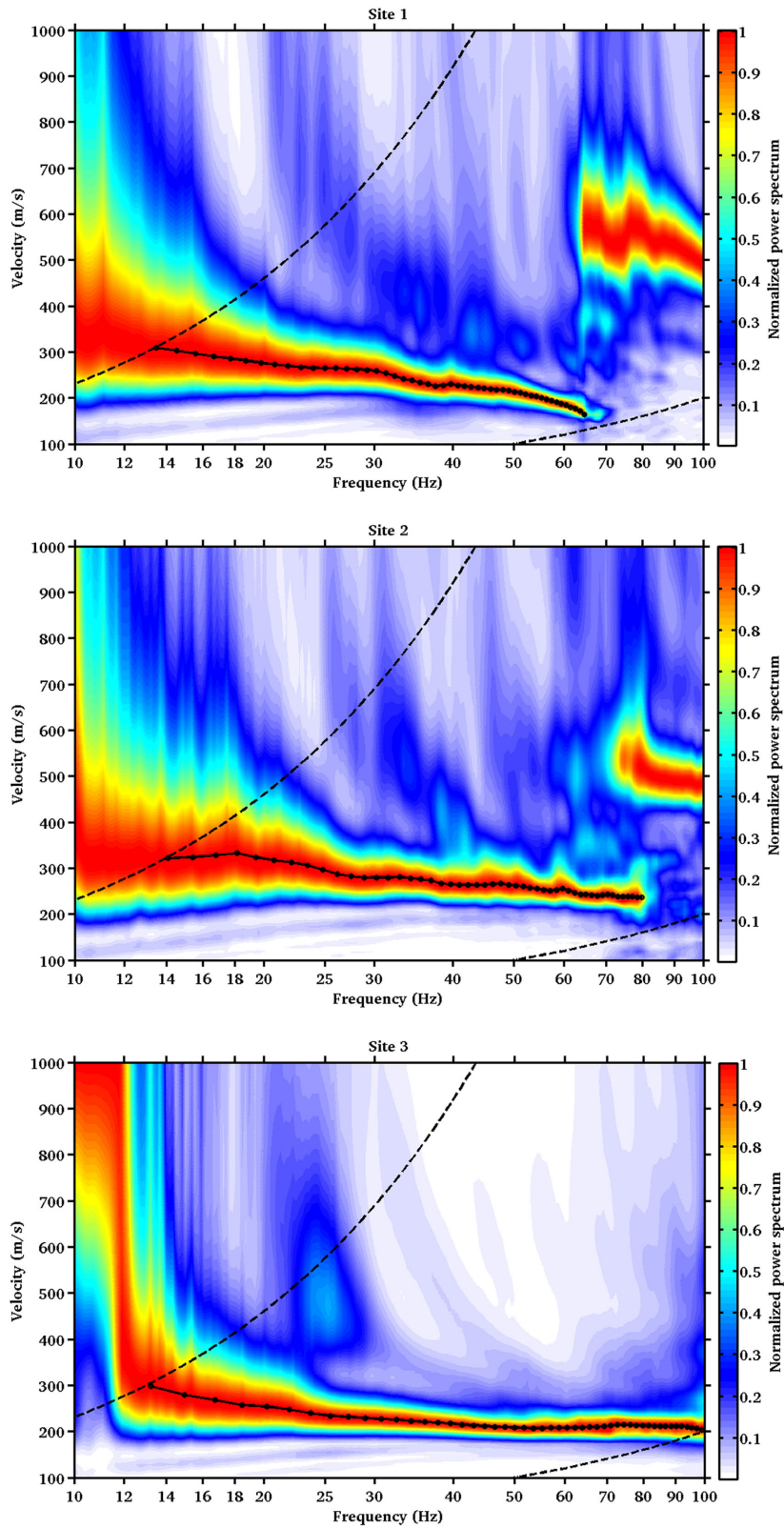

Figure 10. Mapping H/V peak frequencies at Rehab City. Left-hand panel: high-frequency peaks, the varying frequencies indicate different thicknesses of recent sediments. Right-hand panel: low-frequency H/V peaks. The interpolation in some areas is tentative due the low density of measurement points.

Figure 11. Frequency–velocity power spectrum applying conventional beamforming method using 24 geophones at 1 m spacing using 13 shots. Thin dashed black lines define the resolution limits of the method.
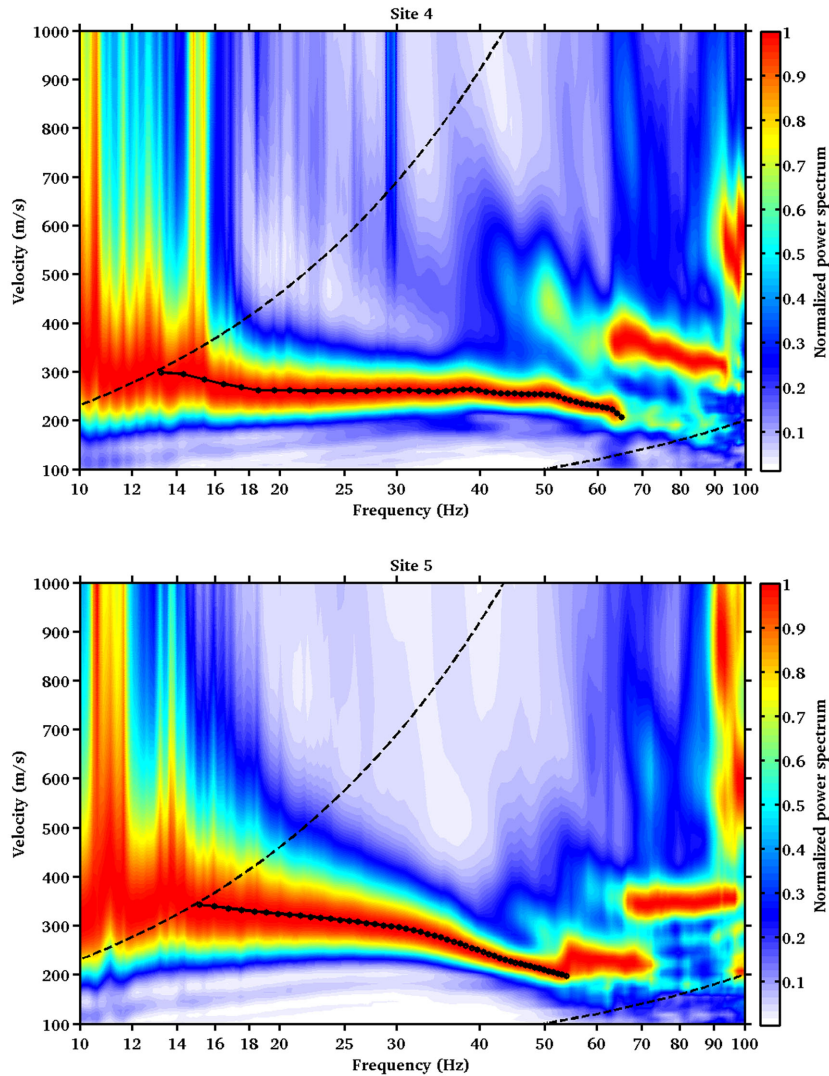
Figure 11. *(Continued.)*

Such behaviour is due to the presence of higher velocity layer below the topmost low-velocity quaternary sediments. This behaviour is in agreement with the documented geological setting of the site, which is composed of a thin layer of shallow quaternary sediments overlying Hagul formation (Said 1992). The dispersion at sites 1, 2 and 4 is similar because these sites share the same type of soil deposits (Gebel Ahmar formation). Identification of higher modes is possible, particularly at high frequencies, but their mode addressing is doubtful. For that reason, higher modes have not been interpreted and used for subsequent inversion. At site 5, for instance, there is an abrupt change of velocity above 50 Hz, which could be potentially interpreted in terms of energy jump from the fundamental to the first higher mode.

6 INVERSION OF SURFACE WAVE DATA

A model of the underlying velocity structure has been derived from Rayleigh wave dispersion curves and ellipticity functions by solution of a geophysical inverse problem. Given the highly non-linear and particularly non-unique nature of the problem to solve, the use of a direct search optimization algorithm is best suited (Ryden & Park

2006; Socco & Boiero 2008). We make use of a modified version of the Neighborhood Algorithm (NA, Sambridge 1999; Wathelet *et al*. 2004) as implemented in the software Dinver (www.geopsy.org). NA is a sampling algorithm that merges the advantage of exploring the model space by a direct random sampling, such as the Monte Carlo method, in addition to directing the search process towards regions of best-fitting model parameters. The original NA algorithm is modified in Dinver to allow irregular limits in the investigated parameter space and dynamic scaling (Wathelet 2008). In addition, the algorithm can account for conditionality of the soil properties, as for the assumption of velocity increasing with depth, which helps to reduce considerably the non-uniqueness of the inverse problem.

With the absence of detailed information about the local structure, the assumed site models should be sufficiently simple and general (in terms of the number of layers) to represent the average complexity of the region. The thickness, density, compressional and shear wave velocity of constituting layers are free parameters of the optimization, constrained within *a priori* defined search bounds. Additional prior constraints are also used, such as limiting the Poisson's ratio to impose a physical conditionality between Vp and Vs.

Table 1. Model parameters of the synthetic data set.

	Thickness (m)	Vp (m s^{-1})	Vs (m s^{-1})	Density (kg m^{-3})
1st layer	2	350	200	1900
2nd layer	10	630	400	1900
3rd layer	25	680	460	1900
4th layer	50	720	500	1900
5th layer	100	760	550	1900
Half-space	–	3900	2400	2500

6.1 Combined inversion of multiple data sets

Due to the limited extension of the array configuration and the typology of adopted active source, application of MASW can just retrieve the dispersion at rather high frequencies, which can only be used as constraint to characterize the topmost parts of the soil structure (Park *et al.* 1998, 1999; Bodet *et al.* 2005; Xia *et al.* 2007; Poggi *et al.* 2013). On the other hand, the ellipticity of Rayleigh waves (at the peak and right flank) is related to the sediment–bedrock interface (Fäh *et al.* 2001, 2003).

Hence, a more realistic representation of the velocity models down to the sediment–rock interface can be retrieved by jointly inverting surface wave dispersion curves and Rayleigh wave ellipticity information from H/V spectral ratios (Nagashima & Maeda 2005; Parolai *et al.* 2005; Picozzi & Albarello 2007; Poggi *et al.* 2012). The retrieved models in this case conform to both of the two data sets. Nonetheless, application of combined inversion can be extended to other information, for example, dispersion curves of Rayleigh and Love waves, fundamental and high-frequency higher modes with the aim of improving resolved models.

In combined inversions, different data sets are assigned different relative weights because they have varying sensitivity to the model parameters. The calibration of the relative weights can be done following a trial-and-error process. Usually, surface wave dispersion is assigned larger weight than the ellipticity peak and right flank. We obtained a satisfactory convergence of the solution with factors 2, 1, and 1, respectively.

6.2 Inversion results

Before inverting the retrieved data set, a synthetic data set of similar characteristics has been used as a benchmark to verify the possibility of retrieving the velocity structure. This data set is composed of Rayleigh wave dispersion data at high frequency (12–50 Hz), plus ellipticity (first peak and right flank) in the range 0.7–1.2 Hz. Artificial uncertainty is prescribed to the ellipticity amplitude and peak frequency assuming a standard deviation of 1.2 and 0.12, respectively. The corresponding velocity structure is composed of five layers overlying a half-space (see Table 1 for detailed model information).

The first step of the inversion process consists of an explorative phase where 5000 soil models are randomly generated within a bounded parameter space (Table 2) and compared with the input data set. The search is then iteratively refined (40 times) by progressively reducing the size of the parameter spaces and generating

additional 100 models at each iteration. Thus, 9000 models are then investigated in total. To explore the non-uniqueness of the inverse problem and to direct the search to low-misfit regions, 10 voronoi cells with the lowest misfit are used to generate new models in each iteration.

To account for the uncertainty of the ellipticity data set, a weighted misfit approach is used where uncertainty of the amplitude of ellipticity functions is considered in the calculation of the misfit according to:

$$M_e = \sqrt{\sum_{i=1}^{N} \frac{\left(\text{ell}_{\text{obs}_i} - \text{ell}_{\text{test}_i}\right)^2}{\sigma_i^2 N}} \qquad (1)$$

where M_e is misfit, $\text{ell}_{\text{test}_i}$ is the amplitude of observed ellipticity right flank at the frequency f_i, $\text{ell}_{\text{test}_i}$ is amplitude of generated ellipticity function at the same frequency, σ_i is the uncertainty of observed data and N is the number of samples. In addition, uncertainty of the peak frequency is considered as in the following equation:

$$M_{f_0} = \frac{\left| f_{0_{\text{obs}}} - f_{0_{\text{test}}} \right|}{\sigma} \qquad (2)$$

where M_{f_0} is the misfit of the peak frequency, $f_{0_{\text{obs}}}$ is the peak frequency of observed ellipticity function, $f_{0_{\text{test}}}$ is the peak frequency of generated ellipticity and σ is the standard deviation of observed peak frequency. However, assuming that MASW results are certain, only the maxima of normalized power spectra are used. For the joint inversion, the total misfit is finally computed by combing the misfits of involved data sets. Following this approach, the set of inverted velocity profiles with sediment–bedrock interface depth between around 170 and 250 m lie within the uncertainty limit of the ellipticity function (Fig. 12).

The experimental data set is composed of dispersion curves at the high frequency and ellipticity information at the low frequency. The dispersion curves resolved the uppermost part of the profile and the ellipticity function constrained the sediment–bedrock interface. Because the middle layers (above the bedrock interface) remain unconstrained, we assumed a power law increase where the velocity increases with depth. This assumption matches the common situations where the velocity usually increases downward by the action of compaction and overburden pressure.

The fitting between observed and calculated dispersion curves is generally very good. The retrieved models are however kept relatively simple. At the top, the quaternary sediments are represented by a thin layer usually of 2–4 m. Gebel Ahmar, Maadi and Hagul formations are represented by four layers (expressing a power law downward increase of velocity). These formations overlie limestone bedrock. Fig. 13 shows the retrieved model at site 1. Considering the uncertainty in the ellipticity function, the ensemble of models with sediment–bedrock interface depth between 180 and 210 m are acceptable.

**Table 2.** Model parametrization applied in the inversion.

Search ranges		Depth (m)	Vp (m s^{-1})	Vs (m s^{-1})	Density (kg m^{-3})
1st layer		1–50	100–700	50–400	1900–2600
2nd layer (four sublayers)	Top	–	150–1000	100–500	
	Bottom	50–300	300–4000	200–2500	
3rd layer		–	2500–5000	1000–3500	
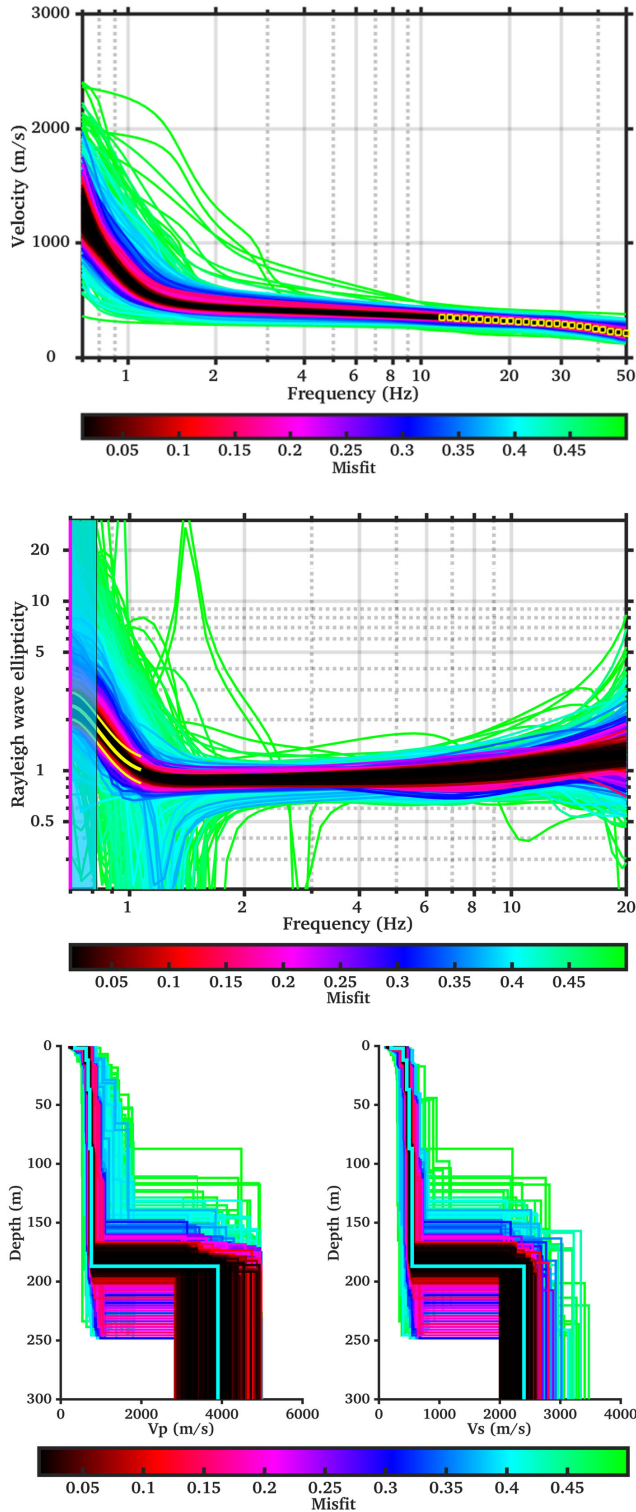
Figure 12. Combined inversion of high-frequency fundamental-mode Rayleigh dispersion curve and ellipticity peak and right flank. Yellow squares represent the dispersion data (upper panel); yellow curves show the mean and uncertainty of the ellipticity right flank and shaded area defines the error in f_0 (middle panel). The cyan line (bottom panel) shows the true model.
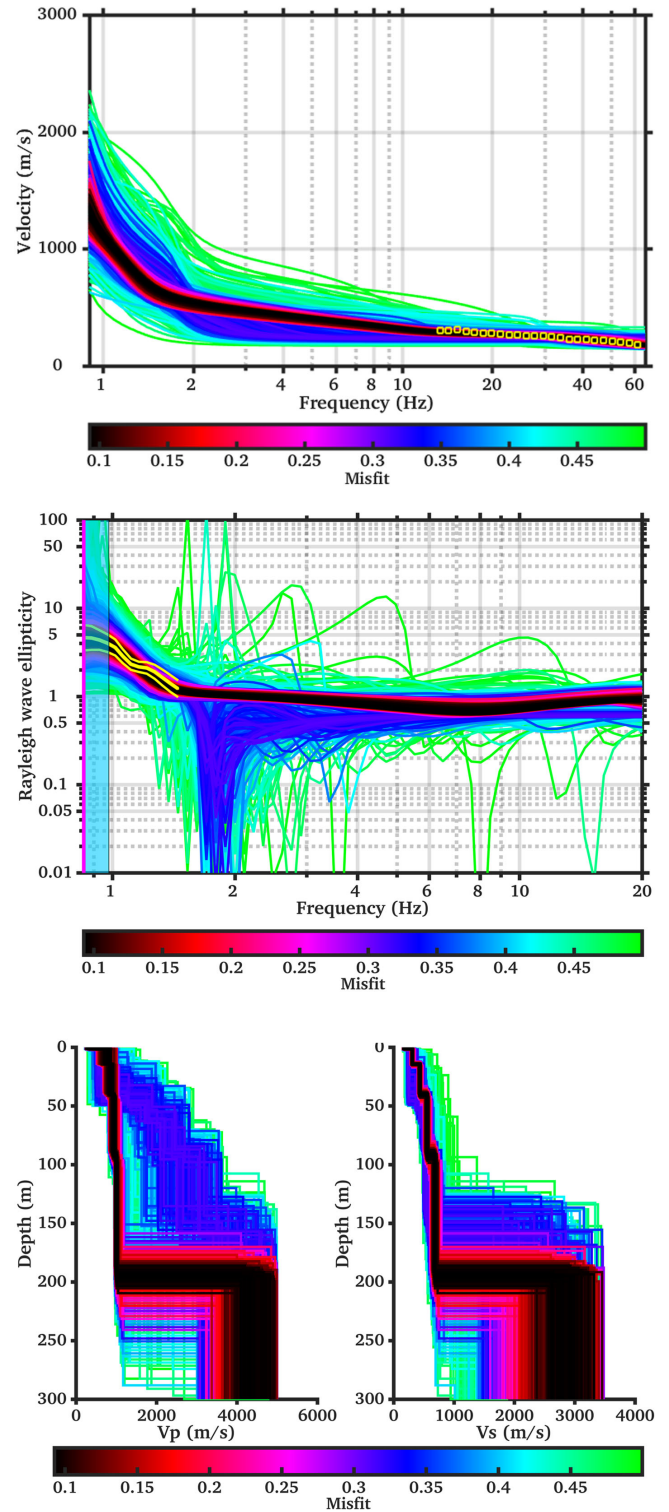
Figure 13. Dispersion, ellipticity and ground model at site 1. Measured dispersion is shown by yellow squares (upper panel), mean and uncertainty of ellipticity right flank in yellow and shaded area defines the error in f_0 (middle panel).
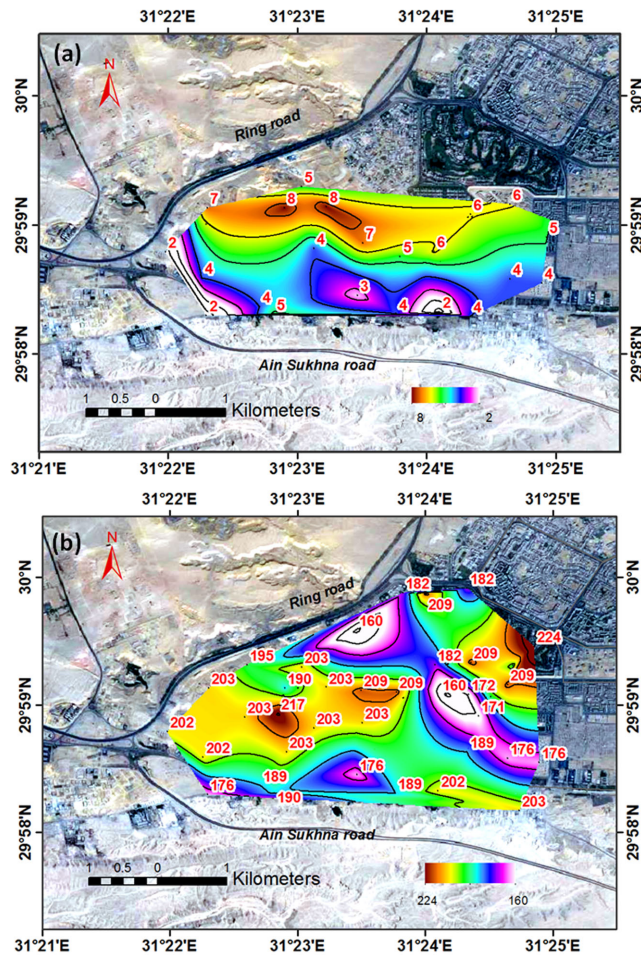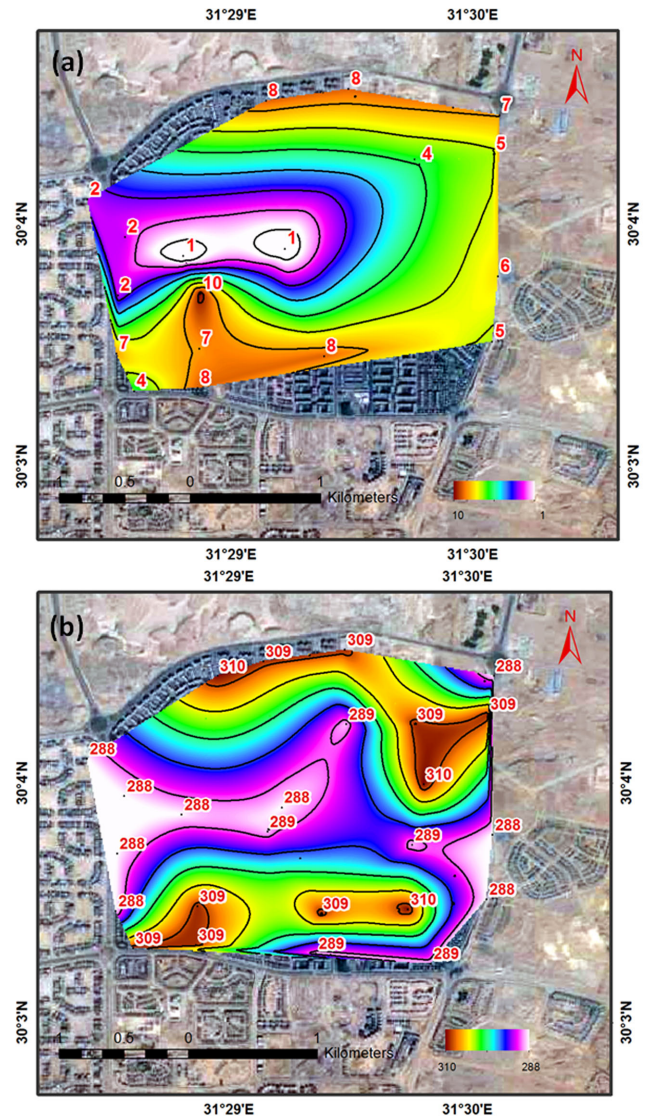
Figure 14. Mapping the depth of shallow (a) and deep (b) interfaces at Kottamiya. The interpolation in some areas is tentative due the low density of measurement points.

7 USING RAYLEIGH WAVE ELLIPTICITY FOR MAPPING BEDROCK DEPTH

At Kottamiya, as previously pointed out, H/V curves exhibit low- and high-frequency peaks induced, respectively, by deep and shallow interfaces with impedance contrasts. Assuming that the low-misfit velocity models represent the average velocity structure over the area, a reasonable estimation of the depth to the interfaces controlling the high- and low-frequency peaks can be obtained. This is achieved by generating the theoretical ellipticity function using the estimated physical properties of the layers above and below the interface of interest. The ellipticity function is then calculated for a broad range of layer thicknesses. The depth of the model corresponding to the ellipticity function that has fundamental frequency, which closely matches that of H/V curves, is selected (Poggi *et al.* 2012). The depth to the shallow interface is first estimated by using the high-frequency peaks (Fig. 14a). Subsequently, the depth to the deeper interface is then estimated (Fig. 14b) using the low-frequency peaks taking into account the variability of the shallow interface obtained in the first step. The depth maps are then generated by repeating this procedure at all H/V locations.

The velocity structure at south Kottamiya (site 3) is different from that at north Kottamiya (site 4). Therefore, the south model is

Figure 15. Mapping the depth of shallow (a) and deep (b) interfaces at Rehab City. The interpolation in some areas is tentative due the low density of measurement points.

used at the locations where we observed the high-frequency peaks; otherwise, we used the north model.

At Rehab City, observed high- and low-frequency peaks are used, respectively, to map shallow and deep interfaces by following the same procedure applied at Kottamiya (Fig. 15). At Zahraa, the high-frequency peaks are missing and therefore there is only one map for the sediment–bedrock interface (Fig. 16). The estimated depths are comparable with the depths of the inverted models at locations of active measurements. However, the estimated 3-D models are affected by uncertainties imposed by the inversion and uncertainties of the ellipticity functions. Low-frequency peaks are sometimes associated with considerable uncertainty especially at Kottamiya. Therefore, the obtained models are considered approximate representations. The obtained models can be enhanced by performing additional field measurements or if other information from boreholes become available to be used as *a priori* information.
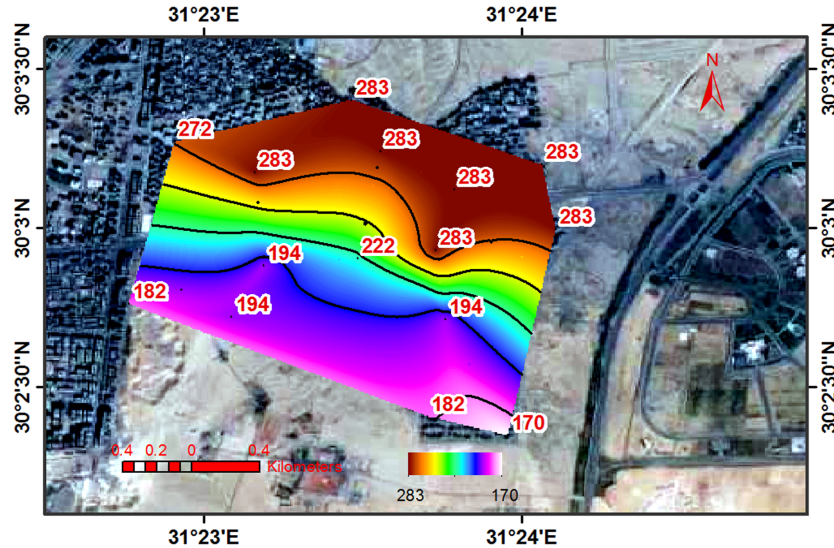
Figure 16. Mapping the bedrock depth at Zahraa. The interpolation in some areas is tentative due the low density of measurement points.

Table 3. Vs in the uppermost part of the soil profile and soil classification at the active MASW sites.

Site number	Vs_{10}	Vs_{20}	Vs_{30}	Vs_{50}	Vs_{100}	Soil class
1	340	377	407	445	505	B
2	337	373	401	437	490	B
3	295	337	366	405	461	B
4	279	322	351	400	476	C
5	351	392	415	444	481	B

8 30 m SHEAR WAVE VELOCITY AND SOIL CLASSIFICATION

For seismic hazard analysis, soil is classified using simplified approaches, such as the shear wave velocity of the upper 30 m of the soil profile (Vs_{30}). The Vs_{30} is calculated by averaging the travel-times (Kanli *et al.* 2006). In the Eurocode 8 (Sabetta & Bommer 2002), five site classes (soil types from A to E) are defined based on Vs_{30}.

Based on the Vs_{30} parameter (Table 3), the study areas generally belong to site class B. Such site class is typically related to sand and gravel deposits and shale and marl occurrences. However, at experiment 4, the soil is related to the C class, and this could be due to recent local infill in West Golf area. Estimates of traveltime average velocity over different depths (Vs_{10}, Vs_{20}, Vs_{30}, Vs_{50} and Vs_{100}), indicate comparable characteristics with other locations at larger depths except at the near surface of site 4 (Table 3), and thus supports the presence of such local infill.

9 GROUND-MOTION AMPLIFICATION MODEL

The seismic waves usually travel long distances through rock layers and finally cross a relatively small thickness of low-velocity sediments before reaching the earth's surface. However, the low-velocity soil deposits can significantly amplify the ground motion at the surface. We use the *SH*-wave transfer function to model the frequency-dependent amplification as described in the following.

9.1 Elastic *SH*-wave transfer function

If the assumption of one-dimensionality holds, the elastic response of the soil can be easily represented by a linear transfer function, where a soil deposit is assumed to behave like a linear elastic system under impulse excitation (Kennett & Kerry 1979; Huang & Wang 1981). In the frequency domain, the soil transfer function can be obtained as the ratio between the ground motion observed at the surface and the bedrock.

However, if no direct observations are available, the theoretical transfer function can be calculated analytically as the solution of the wave equation considering multiple reflections and refractions at different boundaries within the layered system. In this study, we implement the implicit calculation scheme following the Knopoff layer-matrix formulation (Knopoff 1964). The quality factors are estimated following the model proposed by Poggi & Fäh (2015) because there is no information currently available about Q_s in the study area.

9.2 Uncertainty estimation

To account for the uncertainty of the input data (Rayleigh wave ellipticity, in this case) and of the inversion procedure on the final amplification model, we use the model misfit to perform a weighted statistical analysis. As introduced in Section 6.2, the misfit of each inverted velocity profile accounts for the uncertainty of the input data by including their standard deviation (eqs 1 and 2). Therefore, the total misfit can be used as a weighting factor to compute average numerical amplification from the initial 5000 velocity profiles randomly generated within the inversion. We use such weighting scheme to compute the following weighted mean, in lognormal statistic:

$$\bar{A} = e^{\frac{\sum_{i=1}^{N}(M_i)^{-\alpha}\ln(A_i)}{\sum_{i=1}^{N}(M_i)^{-\alpha}}} \tag{3}$$

where $\bar{A}$ is the weighted mean amplification, A_i is the amplification by the model i, M_i is the total misfit of the model i, α is a weighting coefficient and N is the number of models.
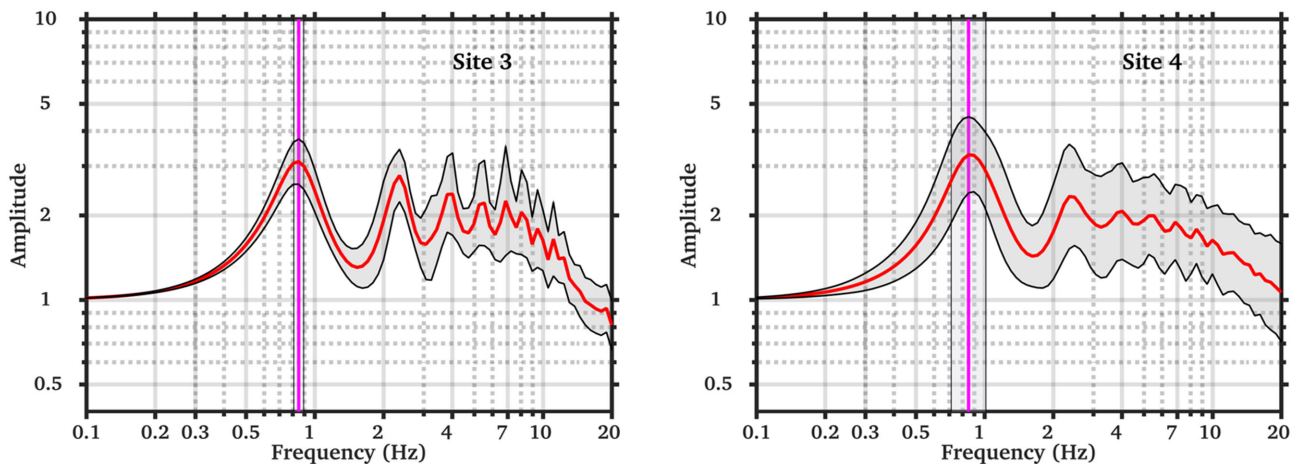
Figure 17. *SH*-wave transfer functions calculated at two sites at Kottamiya. Weighted mean and standard deviation are calculated using eqs (3) and (4).

As well, the amplification weighted standard deviation (SD_W) can be computed as:

$$SD_w = e^{\sqrt{\frac{\sum_{i=1}^{N}(M_i)^{-\alpha}(\ln(A_i)-\ln(\tilde{A}))^2}{\frac{(N-1)\sum_{i=1}^{N}(M_i)^{-\alpha}}{N}}}} . \tag{4}$$

The coefficient α is used to tune the significance and sensitivity given to extreme models (with large misfit). After several trials, we found an optimal balance using a value of -7. It has to be noted, however, that the subjective choice of such sensitivity parameter affects the uncertainty on the resulting average amplification model, which should be then used only qualitatively. Such approach is nonetheless beneficial to perform relative comparison of amplification models between sites of different characteristics.

9.3 Results

Using the developed statistical model, the mean and uncertainty of amplification functions at the locations of active experiments are estimated. The amplification is lower at site 3 in south Kottamiya (Fig. 17) compared to the north of the city (e.g. site 4). This is related to the different stiffness and damping characteristics of the soil deposits where, in the south, the site is composed of successions of marl and shale of Maadi formation, whereas in the north the sites are composed of loose sands of Gebel Ahmar formation. The resulting uncertainty in *SH* amplification is generally in the range $1.2-1.4$ at the resonance frequency. Such uncertainty is higher at north Kottamiya (site 4) than at the southern parts (Fig. 17). To map the amplification across the areas, a 3-D model discretization of the study areas is performed by dividing the areas into a number of local vertical profiles (1-D models) at each H/V measurement location. Subsequently, modeling of *SH*-wave amplification is performed at each H/V measurement location assuming local one-dimensionality of the soil structure and using the low-misfit model.

The amplification factors at the fundamental frequency are mapped across Kottamiya (Fig. 18). Amplification factors up to 5 are observed at Zahraa and Rehab City (not shown) without evident spatial variability because of the more or less homogenous structure.
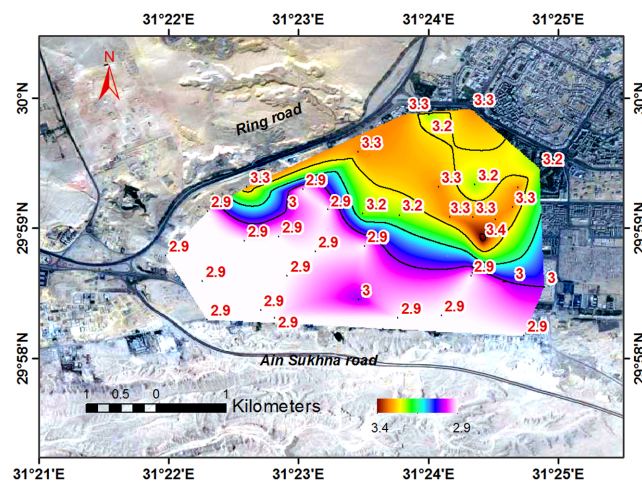

Figure 18. Amplification factors of *SH*-wave transfer function model at the fundamental frequency at Kottamiya.

10 CONCLUSIONS

This study is conducted for retrieving an estimation of the velocity structures in three study areas. The velocity models are used for obtaining the Vs_{30} parameter and for defining the amplification factors for subsequent assessment of the seismic hazard.

Ambient vibrations were recorded at 117 sites and analysed with the single-station H/V method. Additional five linear array active experiments were conducted to retrieve the dispersion curves of Rayleigh waves.

H/V Fourier spectral ratios have been used to estimate Rayleigh wave ellipticity functions in the frequency band around the fundamental frequency. Due to the limitations imposed by the employed source and the array configuration, application of active MASW allows retrieving the dispersion curves at the high frequency only (down to 12–13 Hz). Dispersion curves in the high frequency can just resolve the shallow part of the profile but can constrain the inversion for the shallow structure.

A two-step inversion strategy allows retrieving the velocity structure down to the sediment–bedrock interface. While the dispersion curves are used to resolve the uppermost low-velocity part of the profile, the ellipticity function of Rayleigh waves (peak and right

flank) provided a constraint on the depth of the sediment–bedrock interface. However, these models can be enhanced by performing additional field measurements or if other information from boreholes becomes available to be used as *a priori* in the inversion. On the other hand, the estimated Vs_{30} parameter is considered reliable because the uppermost section of the profile is well resolved by the dispersion curves.

The site models are affected by uncertainties imposed by the inversion, as well as by uncertainties of the ellipticity functions. Considering the latter uncertainty, the ensemble of models that lie within the uncertainty limit of the data set is considered acceptable. Moreover, uncertainty in the empirical ellipticity estimates is used to directly quantify the uncertainty in the site amplification models. A weighted statistical analysis (mean and standard deviation) is performed on the ensemble of amplification functions computed from the inverted velocity models using their misfit as weighting scheme. In this, large significance is given to best-fitting models, while unrealistic models are automatically discarded from the analysis.

The results reveal that the study areas experience frequency-dependent amplification, with largest amplification occurring at the resonance frequencies of the sites. Amplification up to a factor of 5 is found, with some variability observed just in Kottamiya, depending on the soil types and the resonance frequency. Uncertainty in the range 1.2–1.4 in amplification factors is observed at the resonance frequency. Amplification is expected to affect buildings in the frequency band between less than 0.8 and 10 Hz.

ACKNOWLEDGEMENTS

REFERENCES

Abou Elenean, K.M., Hussein, H.M., Abu El-Ata, A.S. & Ibrahim, E.M., 2000. Seismological aspects of the Cairo earthquake, 12th October 1992, *Ann. Geofis.,* **43**(3), 485–504.

Arai, H. & Tokimatsu, K., 2008. Three-dimensional v_s profiling using microtremors in Kushiro, Japan, *Earthq. Eng. Struct. Dyn.,* **37**, 845–859.

Bard, P.Y., 1998. Microtremor measurements: a tool for site effect estimation?, in *Proceeding of the Second International Symposium on the Effects of Surface Geology on Seismic Motion*, Vol. 3, pp. 1251–1279, eds Irikura, K., Kudo, K., Okada, H. & Satasini, T., Rotterdam, Balkema.

Bodet, L., Wijk, K.V., Bitri, A., Abraham, O., Cote, P., Grandjean, G. & Leparoux, D., 2005. Surface-wave inversion limitations from laser-Doppler physical modeling, *J. Environ. Eng. Geophys.,* **10**(2), 151–162.

Bonnefoy-Claudet, S., Cornou, C., Bard, P.Y., Cotton, F., Moczo, P., Kristek, J. & Fäh, D., 2006. H/V ratio: a tool for site effects evaluation. Results from 1-D noise simulations, *Geophys. J. Int.,* **167**, 827–837.

Bonnefoy-Claudet, S., Köhler, A., Cornou, C., Wathelet, M. & Bard, P.Y., 2008. Effects of Love waves on microtremor H/V ratio, *Bull. seism. Soc. Am.,* **98**, 288–300.

Bonnefoy-Claudet, S., Baize, S., Bonilla, L.F., Berge-Thierry, C., Pasten, C.R., Campos, J., Volant, P. & Verdugo, R., 2009. Site effect evaluation in the basin of Santiago de Chile using ambient noise measurements, *Geophys. J. Int.,* **176**, 925–937.

Capon, J., 1969. High resolution frequency wavenumber spectrum analysis, *Proc. IEEE,* **57**, 1408–1418.

Chavez-Garcia, F.J., Sanchez, L.R. & Hatzfeld, D., 1996. Topographic site effects and HVSR. A comparison between observations and theory, *Bull. seism. Soc. Am.,* **86**(5), 1559–1573.

Dal Moro, G., Pipan, M., Forte, E. & Finetti, I., 2003. Determination of Rayleigh wave dispersion curves for near surface applications in unconsolidated sediments, in *International Exposition and Seventy-Third Annual Meeting, Expanded Abstracts*, pp. 1247–1250, Society of Exploration Geophysicists.

Dravinski, M., Ding, G. & Wen, K.L., 1996. Analysis of spectral ratios for estimating ground motion in deep basins, *Bull. seism. Soc. Am.,* **86**(3), 646–654.

Ducellier, A., Kawase, H. & Matsushima, S., 2012. Velocity structure inversion from H/V spectral ratios of earthquake data: application to the Tohoku region, Japan, in *15th World Conference on Earthquake Engineering (15th WCEE),* Lisbon, Portugal (hal-00723850v2).

Endrun, B., 2011. Love wave contribution to the ambient vibration H/V amplitude peak observed with array measurements, *J. Seismol.,* **15**, 443–472.

Fäh, D., Kind, F. & Giardini, D., 2001. A theoretical investigation of average H/V ratios, *Geophys. J. Int.,* **145**, 535–549.

Fäh, D., Kind, F. & Giardini, D., 2003. Inversion of local S-wave velocity structures from average H/V ratios, and their use for the estimation of site-effects, *J. Seismol.,* **7**, 449–467.

Fäh, D., Stamm, G. & Havenith, H.B., 2008. Analysis of three-component ambient vibration array measurements, *Geophys. J. Int.,* **172**, 199–213.

Foti, S., 2000. Multistation methods for geotechnical characterization using surface waves, *PhD thesis*, Politecnico di Torino, Italy.

Haghshenas, E., Bard, P.Y. & Theodulidis, N. & SESAME WP04 Team, 2008. Empirical evaluation of microtremor H/V spectral ratio, *Bull. Earthq. Eng.,* **6**(1), 75–108.

Gouveia, F., Lopes, I. & Gomes, R.C., 2016. Deeper Vs profile from joint analysis of Rayleigh wave data, *Eng. Geol.,* **202**, 85–98.

Hobiger, M., Bard, P.Y., Cornou, C. & Le Bihan, N., 2009. Single station determination of Rayleigh wave ellipticity by using the random decrement technique (RayDec), *Geophys. Res. Lett.,* **36**, L14303, doi:10.1029/2009GL038863.

Hobiger, M., Le Bihan, N., Cornou, C. & Bard, P.Y., 2012. Multicomponent signal processing for Rayleigh wave ellipticity estimation, *IEEE Signal Process. Mag.,* **29**, 29–39.

Hobiger, M. *et al.*, 2013. Ground structure imaging by inversions of Rayleigh wave ellipticity: sensitivity analysis and application to European strong-motion sites, *Geophys. J. Int.,* **192**, 207–229.

Huang, H.L. & Wang, C., 1981. The explicit crustal transfer function for SH-waves by ray theory—the case of one and two layers, *Geophys. J. R. astr. Soc.,* **67**, 649–660.

Kanli, A.I., Tildy, P., Pronay, Z., Pinar, A. & Hermann, L., 2006. Vs30 mapping and soil classification for seismic site effect evaluation in Dinar region, SW Turkey, *Geophys. J. Int.,* **165**, 223–235.

Kennett, B.L.N. & Kerry, N.J., 1979. Seismic waves in a stratified half space, *Geophys. J. R. astr. Soc.,* **57**, 557–583.

Knopoff, L., 1964. A matrix method for elastic wave problems, *Bull. seism. Soc. Am.,* **54**, 431–438.

Köhler, A., Ohrnberger, M., Scherbaum, F., Wathelet, M. & Cornou, C., 2007. Assessing the reliability of the modified three-component spatial autocorrelation technique, *Geophys. J. Int.,* **168**, 779–796.

Konno, K. & Ohmachi, T., 1998. Ground-motion characteristics estimated from spectral ratio between horizontal and vertical components of microtremor, *Bull seism. Soc. Am.,* **88**, 228–241.

Lachet, C. & Bard, P.Y., 1994. Numerical and theoretical investigations on the possibilities and limitations of Nakamura's technique, *J. Phys. Earth,* **42**, 377–397.

Lachet, C., Hatzfeld, D., Bard, P.Y., Theodulidis, N., Papaioannou, C. & Savvaidis, A., 1996. Site effects and microzonation in the city of Thessaloniki (Greece): comparison of different approaches, *Bull. seism. Soc. Am.,* **86**, 1692–1703.

Lacoss, R.T., Kelly, E.J. & Toksoz, M.N., 1969. Estimation of seismic noise structure using arrays, *Geophysics,* **34,** 21–38.

Malischewsky, P.G. & Scherbaum, F., 2004. Love's formula and H/V–ratio (ellipticity) of Rayleigh waves, *Wave Motion,* **40,** 57–67.

Nagashima, E. & Maeda, T., 2005. Inversion analysis on surface wave dispersion curves and H/V spectra by neighbourhood algorithm, in *6th World Congress of Structural and Multidisciplinary Optimization,* Rio de Janeiro, Brazil.

Nakamura, Y., 1989. A method for dynamic characteristics estimation of subsurface using microtremor on the ground surface, *Q. Rep. Railw. Tech. Res. Inst.,* **30**(1), 25–33.

Nogoshi, M. & Igarashi, T., 1971. On the amplitude characteristics of microtremor (part 2) (in Japanese with English abstract), *J. seism. Soc Japan,* **24,** 26–40.

Park, C.B., Miller, R.D. & Xia, J., 1998. Imaging dispersion curves of surface waves on multi-channel record, in *68th Ann. Inter. Mtg. Soc. Expl. Geophys. Expanded Abstracts*, pp. 1377–1380, doi:10.1190/1.1820161.

Park, C.B., Miller, R.D. & Xia, J., 1999. Multichannel analysis of surface waves, *Geophysics,* **64,** 800–808.

Parolai, S., Picozzi, M., Richwalski, S.M. & Milkereit, C., 2005. Joint inversion of phase velocity dispersion and H/V ratio curves from seismic noise recordings using a genetic algorithm, considering higher modes, *Geophys. Res. Lett.,* **32,** L01303, doi:10.1029/2004GL021115.

Picozzi, M. & Albarello, D., 2007. Combining genetic and linearized algorithms for a two-step joint inversion of Rayleigh wave dispersion and H/V spectral ratio curves, *Geophys. J. Int.,* **169,** 189–200.

Picozzi, M., Parolai, S. & Richwalski, S.M., 2005. Joint inversion of H/V ratios and dispersion curves from seismic noise: estimating the S-wave velocity of bedrock, *Geophys. Res. Lett.,* **32,** L11308, doi:10.1029/2005GL022878.

Poggi, V. & Fäh, D., 2015. A proposal for horizontal and vertical elastic design spectra. Input for the new Swiss code for dams. Swiss Seismological Service, ETH Zurich. Tech. Rep. SED/BFE/R/01/06072015.

Poggi, V., Fäh, D., Burjanek, J. & Giardini, D., 2012. The use of Rayleigh-wave ellipticity for site-specific hazard assessment and microzonation: application to the city of Lucerne, Switzerland, *Geophys. J. Int.,* **188,** 1154–1172.

Poggi, V., Fäh, D. & Giardini, D., 2013. Time–frequency–wavenumber analysis of surface waves using the continuous wavelet transform, *Pure appl. Geophys.,* **170,** 319–335.

Roten, D. & Fäh, D., 2007. A combined inversion of Rayleigh wave dispersion and 2-D resonance frequencies, *Geophys. J. Int.,* **168,** 1261–1275.

Ryden, N. & Park, C.B., 2006. Inversion of surface waves using phase velocity spectra, *Geophysics,* **71,** 49–58.

Said, R., 1992. *The Geology of Egypt,* Balkema Press.

Sambridge, M., 1999. Geophysical inversion with a neighbourhood algorithm I. Searching a parameter space, *Geophys. J. Int.,* **103,** 4839–4878.

Sabetta, F. & Bommer, J., 2002. Modification of the spectral shapes and subsoil conditions in Eurocode 8, in *12th Europ. Conf. Earthq. Eng.*, London, Paper ref. 518, Elsevier Science.

Shukry, N.M. & Ayouty, M.K., 1956. The geology of Gebel Iweibid-Gafra area, Cairo-Suez district, *Bull. Soc. Geograph. Egypt.,* **29,** 67–109.

Socco, L.V. & Boiero, D., 2008. Improved monte carlo inversion of surface wave data, *Geophys. Prospect.,* **56,** 357–371.

Tokeshi, J.C., Sugimura, Y. & Karkee, M.B., 2000. Parametric study on simulated microtremors and its application to interpretation of microtremor records, *J. Constr. Struct. Eng. AIJ,* **535,** 69–78.

Uebayashi, H., 2003. Extrapolation of irregular subsurface structures using the horizontal-to-vertical ratio of long-period microtremors, *Bull. seism. Soc. Am.,* **93,** 570–582.

Wathelet, M., 2008. An improved neighborhood algorithm: parameter conditions and dynamic scaling, *Geophys. Res. Lett.,* **35,** L09301, doi:10.1029/2008GL033256.

Wathelet, M., Jongmans, D. & Ohrnberger, M., 2004. Surface wave inversion using a direct search algorithm and its application to ambient vibration measurements, *Near Surf. Geophys.,* **2,** 211–221.

Xia, J., Xu, Y. & Miller, R.D., 2007. Generating an image of dispersive energy by frequency decomposition and slant stacking, *Pure appl. Geophys.,* **164,** 941–956.

Yilmaz, Ö., 1987. *Seismic Data Processing,* Society of Exploration Geophysicists.

Yoon, S., 2011. Combined active-passive surface wave measurements at five sites in the Western and Southern US, *J. Civil Eng.,* **15**(5), 823–830.